Journal of Catalysis 345 (2017) 170–182

Contents lists available at ScienceDirect

Journal of Catalysis

journal homepage: www.elsevier.com/locate/jcat

Single-site zinc on silica catalysts for propylene hydrogenation and propane dehydrogenation: Synthesis and reactivity evaluation using an integrated atomic layer deposition-catalysis instrument

Jeffrey Camacho-Bunquin [a], Payoli Aich [a,b], Magali Ferrandon [a], Andrew "Bean" Getsoian [a], Ujjal Das [a], Fulya Dogan [a], Larry A. Curtiss [a], Jeffrey T. Miller [a,c], Christopher L. Marshall [a], Adam S. Hock [a,d,*], Peter C. Stair [a,e]

[a] Argonne National Laboratory, Lemont, IL 60439, USA
[b] University of Illinois at Chicago, Chicago, IL 60607, USA
[c] Purdue University, West Lafayette, IN 47907, USA
[d] Illinois Institute of Technology, Chicago, IL 60616, USA
[e] Northwestern University, Evanston, IL 60208, USA

ARTICLE INFO

Article history:
Received 16 August 2016
Revised 18 October 2016
Accepted 20 October 2016
Available online 10 December 2016

Keywords:
Hydrogenation
Dehydrogenation
Atomic layer deposition
Zinc

ABSTRACT

Alkyl-zinc and zinc oxide-type sites were synthesized via atomic layer deposition on high-surface-area silica using an integrated atomic layer deposition-catalysis instrument (I-ALD-CAT). One-cycle ALD experiments using diethylzinc (DEZ) afforded Zn/SiO_2 systems that provided key insights into the reactivity and stability of Zn sites as a function of dispersion at the submonolayer level. The I-ALD-CAT tool design allowed for systematic comparison of the reactivity of different grafted zinc sites. Open-shell 16-electron, tricoordinate ethyl zinc-silica sites exhibit higher activity in propane hydrogenation-dehydrogenation compared to 18-electron, tetracoordinate zinc oxide-type centers. Silica surface saturation with Zn(II) sites (~75% of a monolayer) results in facile zinc agglomeration and catalyst deactivation under reaction conditions. Reduced DEZ dosing coupled with thermal substrate pretreatment techniques (e.g., dehydration under vacuum) resulted in increased Zn dispersion and produced Zn/SiO_2 catalysts with improved activity and stability under propylene hydrogenation (200 °C) and propane dehydrogenation (550 °C) conditions.

1. Introduction

Single-site heterogeneous catalysis remains a rapidly growing area due to its potential to combine the tunability of molecular catalysts with the stability of heterogeneous materials under a range of process conditions (e.g., temperature, pressure, solvent) [1,2]. Systematic investigation of active site formation during synthesis and the transformations these species and reactive intermediates undergo during catalysis can harness key structural and mechanistic insights that are essential for the purposeful design of robust single-site catalysts with improved efficiency. However, systematic study of the transformations that these isolated sites undergo remains challenging due to the limitations of the synthesis procedures (e.g., formation of a distribution of sites), and the difficulty in handling sensitive catalytic species and intermediates from synthesis to the reactivity testing stage. Ideally, strategies integrating high-precision active site synthesis methods with immediate catalyst performance testing could allow for the systematic investigation of the catalytic properties of these supported sites without material decomposition from air- or moisture exposure.

In order to prepare single-site catalysts that are uniform in function, they must be synthesized using atomic-level control [3,4]. Recent advances in synthesis techniques have produced catalytic materials with much improved activity, selectivity and stability [5–9]. One thing all of these synthesis methods (e.g., impregnation, ion-exchange, precipitation, organometallic grafting) still lack in many cases is control of the structure, producing materials with a distribution of active sites, which in turn impacts performance. In principle, **A**tomic **L**ayer **D**eposition (ALD) is a high-precision grafting technique that can synthesize a variety of supported catalytic sites (e.g., single atoms or clusters) at the atomic/monolayer level [3,10,11]. ALD is a vapor-phase grafting

* Corresponding author at: Illinois Institute of Technology, Chicago, IL 60616, USA.
E-mail address: ahock@iit.edu (A.S. Hock).

http://dx.doi.org/10.1016/j.jcat.2016.10.017
0021-9517/

method that relies on a stoichiometric and thus self-limiting reaction of chemical precursors with substrate surface functionalities [5–12]. The self-limiting nature of the ALD process presents a number of synthetic advantages that include (1) uniform active site dispersion, (2) high conformity to surface features which, in certain cases, allows for maximum utilization of the support surface area, and (3) high level of reproducibility [3].

Although ALD as a catalyst synthesis tool has been applied mainly for the controlled synthesis of supported bulk – *nanoscale in size* – structures such as metal particles [13], films [14], alloys [15] and core-shell nanoparticles [16], it comprises an ideal strategy for accessing supported single-site catalysts since *the initial nucleation of sites during ALD should consist of isolated sites.* So far, only a few reports of ALD for single-atom catalysts have appeared [17]. Hence, improved understanding of synthesis mechanisms and optimization of key factors for the design of effective ALD synthesis methods to access single sites is warranted.

Our group recently reported the synthesis of isolated, low-coordinate Zn(II) sites on silica via strong electrostatic adsorption. These sites were shown active toward propylene hydrogenation (200 °C) and selective propane dehydrogenation (550 °C). Computational studies revealed the involvement of tricoordinate Zn(II) sites and an alkyl-zinc intermediate in the catalytic cycle (Fig. 1). However, systematic comparison of the intrinsic reactivity of these intermediates remains challenging due to difficulties in the synthesis, and the inherent instability of the species on oxide supports.

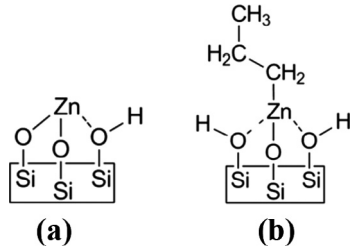

Fig. 1. Proposed reactive intermediates for a previously reported single-site Zn(II)/SiO_2 catalyst for propylene hydrogenation and propane dehydrogenation: (a) three-coordinate Zn(II) site and (b) alkyl-zinc species.

In this paper, we report the use of an **I**ntegrated **A**tomic **L**ayer **D**eposition-**Cat**alysis (I-ALD-CAT, Fig. 2) [18] synthesis and catalyst reaction testing tool for the synthesis of isolated alkyl-zinc and zinc oxide-type sites via one-cycle ALD methods and immediate *in situ* evaluation of the reactivity of these sites at the atomic-scale/submonolayer level under propylene hydrogenation and propane dehydrogenation conditions [18]. The I-ALD-CAT tool – *the first of its kind* – has the capability of (1) ALD synthesis on a support loaded into a plug-flow reactor, a design element that allows for (2) immediate *in situ* catalyst performance evaluation under plug-flow conditions *without material exposure to air or moisture* (Fig. 2).

The approach presented in this report provides key insights into the mechanism of zinc grafting on hydroxylated supports, and the reactivity and stability of these alkyl-zinc and zinc oxide-type sites as a function of zinc dispersion and nuclearity. Additionally, this study presents the use of an organo-zinc pre-catalyst where the initial pre-catalyst ligand (ethyl, C2) is well differentiated from the reacting alkene/alkane (propylene and propene, both C3 species). This approach allowed for the unambiguous monitoring of the activation pathways that the pre-catalyst undergoes during catalysis. Based on this understanding, optimized synthesis of Zn/SiO_2 catalysts with improved activity and stability have been achieved by ALD.

2. Experimental section

2.1. General ALD synthesis conditions

Silica (SiO_2, Davisil 646, 40–50 mesh, 300 m^2/g (BET surface area) and 1.1 cc/g, Sigma-Aldrich) was used as substrate for the gas-phase grafting of Zn catalysts. The synthesis was performed using an ARRADIANCE Integrated ALD-Catalysis tool (model ARR-100000 GEMSTAR-CAT Dual System). A series of ALD experiments were carried out to ensure the self-limiting nature of the gas-phase deposition reaction (see details in the Supporting Information). 160–320 mg of SiO_2 was loaded into a 406 mm × 7 mm (i.d.) stainless steel, plug-flow tube reactor. Unless otherwise stated, the silica substrate for each ALD synthesis experiment was purged with N_2 (10 sccm) for 30 min after reactor tube installation, and subsequently heated at 200 °C for 1 h under vacuum (0.1 Torr). (Note:

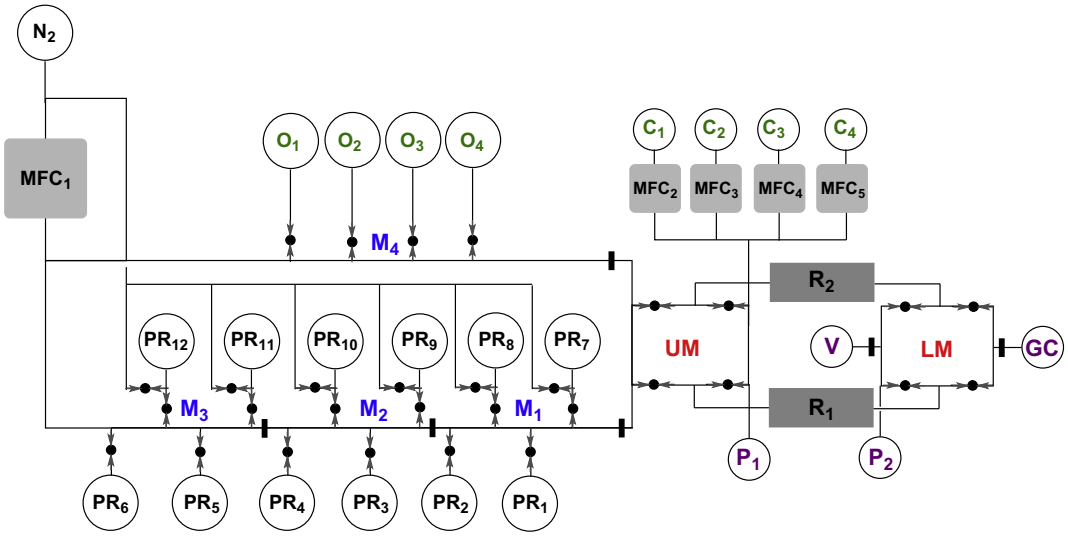

Fig. 2. Schematic diagram for the I-ALD-CAT tool. Lower left: Metal precursors (PR_1–PR_{12}). Upper left: Oxidizing/reducing reagents (O_1–O_4). Upper right: Catalysis reagents (C_1–C_4). Middle right: Plug-flow reactors (R_1, R_2). Middle far-right: Product manifold (LM). The I-ALD-CAT has the capability of providing gaseous reagents comprised of 12 different ALD precursors, 4 oxidizing or reducing agents, and 4 catalytic reaction feeds to the two plug-flow reactors. The reactor is able to immediately test these single site catalysts (or any newly synthesized materials) on a wide range of reactions and process conditions. Volatile products of the ALD synthesis and catalytic reactions can be analyzed by both GC and mass spectrometry [18].

Silica pretreated under the given conditions is reported to have surface hydroxyl density of 4.9 α-OH/nm^2; 2.44 mmol α-OH/g) [19–21]. Diethylzinc (DEZ, >52 wt.% Zn basis, Sigma-Aldrich) as the Zn ALD precursor and, in some cases, deionized H_2O was used to protonate the organo-zinc intermediates. Reported thermal growth windows for DEZ–H_2O ALD range from 25 to 200 °C [22]. The ALD experiments in this study were carried out at 100 and 175 °C (Note: The substrate temperature reported in this study is temperature reading of the thermocouple attached to the reactor chamber. The actual silica bed temperature is not measured during the ALD process). During the course of ALD synthesis, the manifold upstream of the reactor chamber (**M_1–M_3, UM**) was maintained at 135 °C, the valves downstream of the reactor (**LM**) at 175 °C. Both the DEZ and H_2O bottles were kept at ambient temperature during the synthesis. Each ALD precursor pulse was carried out in a three-step sequence: (1) manifold evacuation to 1 Torr base pressure (30 s), (2) precursor pulse (10–25 ms) at 1 Torr pressure, and (3) 50 sccm N_2 purge (30 s). The progress of the deposition experiment was monitored by detection of ethane using an online residual gas mass spectrometer. (Note: The rate of DEZ delivery is estimated to be 110 mg (0.89 mmol) DEZ/Torr-s. This number is based on the consumption of 5 g of DEZ over 45 Torr-s). ICP-AES analysis of Zn/SiO_2 samples was conducted by Galbraith Laboratories, Inc. (Knoxville, TN) to determine the zinc loading (per weight basis).

2.1.1. Zn_A [(60 × 25 ms) DEZ–(60 × 25 ms) H_2O; 175 °C]

One cycle deposition of ZnO was carried out using 60 consecutive 25 ms (1 Torr) pulses of DEZ followed by 60 consecutive 25 ms (1 Torr) pulses of H_2O on 160 mg SiO_2 (0.39 mmol α-OH) [19,21]. Ethane generation during the DEZ pulsing experiments indicates that saturation coverage of the SiO_2 substrate by DEZ is achieved within the first 30 pulses.

2.1.2. Zn_B [(30 × 25 ms) DEZ–(30 × 25 ms) H_2O; 175 °C]

One-cycle ZnO deposition was carried out using 30 consecutive 25 ms (1 Torr) pulses of DEZ followed by 30 consecutive 25 ms (1 Torr) pulses of H_2O on 160 mg SiO_2 (0.39 mmol α-OH).

2.1.3. Zn_C 3[(30 × 25 ms) DEZ–(30 × 25 ms) H_2O; 175 °C]

Three cycles of zinc oxide deposition were carried out on 160 mg SiO_2 (0.39 mmol α-OH 30 consecutive 25 ms (1 Torr) DEZ pulses followed by 30 consecutive 25 ms (1 Torr).

2.1.4. Zn_D 10[(30 × 25 ms) DEZ–(30 × 25 ms) H_2O; 175 °C]

Ten cycles of zinc oxide deposition were carried out on 160 mg SiO_2 (0.39 mmol α-OH 30 consecutive 25 ms (1 Torr) DEZ pulses followed by 30 consecutive 25 ms (1 Torr) H_2O.

2.1.5. Zn_E (30 × 25 ms DEZ; 175 °C)

One-cycle DEZ deposition was carried out using 30 consecutive 25 ms (1 Torr) pulses of DEZ on 160 mg SiO_2 (0.39 mmol α-OH).

2.1.6. Zn_F (30 × 10 ms DEZ; 175 °C)

One-cycle DEZ deposition was carried out using 30 consecutive 10 ms (1 Torr) pulses of DEZ on 320 mg SiO_2 (0.78 mmol α-OH).

2.1.7. Zn_G (30 × 10 ms DEZ; 175 °C)

The silica substrate for this experiment was dehydrated at 600 °C under vacuum (0.1 Torr) for 1.5 h prior to the ALD experiment. SiO_2 dehydration at 600 °C results in α-OH concentration of 1.5/nm^2 (0.75 mmol α-OH/g). One-cycle DEZ deposition was carried out using 30 consecutive 10 ms (1 Torr) pulses of DEZ on 320 mg SiO_2 (0.24 mmol α-OH).

2.1.8. Zn_H (30 × 10 ms DEZ; 100 °C)

One-cycle DEZ deposition was carried out using 30 consecutive 10 ms (1 Torr) pulses of DEZ on 320 mg SiO_2 (0.78 mmol α-OH).

2.1.9. Zn_{Et}, SiO_2-Zn—CH_2CH_3 synthesis by solution grafting

Solution grafting of DEZ on silica was conducted inside a N_2 glove box. A 20 mL scintillation vial was charged with 500 mg SiO_2 (1.22 mmol α-OH); SiO_2 dehydrated at 200 °C prior to solution grafting) [19,21]. A 2 mL mixed hexanes solution containing 176 mg (1.42 mmol) DEZ was then added to the resulting mixture dropwise with constant stirring at room temperature. The reaction mixture was allowed to stir for three hours after the complete addition of DEZ. The resulting mixture was then filtered through a ceramic filter frit and washed three times with 5 mL portions of hexane. The residue was then dried *in vacuo* for six hours. The product was characterized by elemental analysis (%Zn and C), infrared spectroscopy, X-ray absorption spectroscopy and solid-state, multinuclear (^{1}H, ^{13}C, ^{29}Si) magic-angle spinning NMR spectroscopy.

2.2. I-ALD-CAT in situ catalysis studies

The *in situ* catalyst reactivity experiments were conducted immediately after each ALD catalyst synthesis by switching the I-ALD-CAT tool to "catalysis mode." On-line GC analyses were performed using an Agilent 7890 equipped with a 6-port injection valve, a split/splitless injector and a flame ionization detector. A 60 m × 0.32 mm GS GasPro capillary column was employed for the separation. GC cycle times were typically 8 min. In a typical test, 160 to 320 mg of catalyst generated from the *in situ* ALD synthesis was tested.

2.2.1. Propylene hydrogenation

The ALD-synthesized ZnO-type catalyst candidates (Zn_{A-D}) and the reference catalyst Zn_{SEA}, were activated with 2.5 mol% H_2 in He (Airgas USA, LLC), purified using an oxygen trap, at 40 mL/min at 200 °C for 30 min. After the H_2-treatment, the catalyst was fed with 10 mL/min 3.0 mol% propylene in N_2, maintaining the initial 40 mL/min H_2 flow. Since the study aims to differentiate the activity of ZnO- and organozinc-type sites, the supported ethyl-zinc catalysts (Zn_{E-H}) were tested immediately after the ALD synthesis without a H_2 pretreatment step. After the ALD synthesis of the catalyst, the reactor temperature was increased to the desired temperature and was fed with 10 mL/min 3.0 mol% propylene in N_2 and 40 mL/min H_2 flow.

2.2.2. Propane dehydrogenation

The reference catalyst Zn_{SEA} was heated to 200 °C for 30 min, maintaining a 40 mL/min flow of a 2.5 mol% H_2 feed. The reactor was then heated to 550 °C until the temperature is stable, and then fed with 2.5% propane/Ar at 10 mL/min. The supported ethyl-zinc catalyst (Zn_F) was tested immediately after the ALD synthesis. The reactor temperature was increased to 550 °C with a constant 40 mL/min flow of N_2. When the temperature stabilized, the reactor was fed with 2.5% propane/Ar at 10 mL/min.

2.3. Infrared spectroscopy

Infrared (IR) spectra were collected using a Bruker Alpha FTIR spectrometer (Bruker Optics, Billerica, MA) under DRIFTS mode. Spectra at 4 cm^{-1} resolution were obtained in absorbance mode over the 375–4000 cm^{-1} range. Air-sensitive samples were characterized in a glove box under a nitrogen atmosphere. All IR data were normalized, baseline-corrected, and analyzed using OPUS (v7.0, Bruker Optics, Billerica, MA) software.

2.4. Solid-state proton magic-angle spinning (^{1}H MAS) NMR spectroscopy

Air-sensitive samples were packed into a 1.3 mm rotor post vacuum dry under an Argon atmosphere. ^{1}H/^{13}C Cross-Polarization (CP) and ^{1}H Single Pulse Magic Angle Spinning (MAS) Solid-State NMR experiments were performed at 11.7 Tesla on a Bruker Avance spectrometer, operating at Larmor frequencies of 500.13 MHz for ^{1}H and 125.76 MHz for ^{13}C, using a 2.5 mm MAS probe. ^{1}H/^{13}C CP MAS spectrum was measured at a spinning speed of 20 kHz, with a contact time of 4 ms and a recycle delay of 2 s. The RF field strengths for ^{1}H ^{13}C CP experiment were ~83.3 and ~73.5 kHz for ^{1}H and ^{13}C, respectively. SPINAL-64 was applied as a heteronuclear decoupling sequence. ^{1}H single pulse experiment was performed at a spinning speed of 20 kHz, with a $\pi/2$ pulse of 2.5 μs and a recycle delay of 2 s. ^{1}H/^{29}Si Cross Polarization (CP) and ^{29}Si Single Pulse Magic Angle Spinning (MAS) Solid-State NMR experiments were performed at 7.05 Tesla on a Bruker Avance III HD spectrometer, operating at Larmor frequencies of 300.13 MHz for ^{1}H and 59.62 MHz for ^{29}Si, using a 3.2 mm MAS probe. ^{1}H/^{29}Si CP MAS spectrum was measured at a spinning speed of 10 kHz, with a contact time of 4 ms and a recycle delay of 2 s. The RF field strengths for ^{1}H ^{29}Si CP experiment were ~72 and ~42.5 kHz for ^{1}H and ^{29}Si, respectively. SPINAL-64 was applied as a heteronuclear decoupling sequence. ^{29}Si single pulse experiment was performed at a spinning speed of 10 kHz, with a $\pi/2$ pulse of 5 μs and a recycle delay of 30 s. In all experiments ^{1}H, ^{13}C and ^{29}Si chemical shifts were referenced to TMS at 0 ppm and the sample was packed into NMR rotor under an inert atmosphere in a glove box.

2.5. X-ray absorption spectroscopy

X-ray absorption spectroscopic characterization (XAS) of various Zn/SiO_2 samples was conducted by Zn K-edge (9.659 keV) measurements on the bending magnet beamline of the Materials Research Collaborative Access Team (MRCAT, 10-BM) at the Advanced Photon Source (APS), Argonne National Laboratory. The Zn/SiO_2 samples were pressed into 4 mm self-supporting wafers and placed in a stainless steel holder. The air-sensitive SiO_2-Zn—CH_2CH_3 sample prepared by solution grafting was prepared inside a glove box under a N_2 atmosphere, and maintained under air-free conditions throughout the course of the XAS measurement. Each stainless steel holder was placed into a quartz tube (1 in. o.d., 10 in. length) reactor capped with Ultra-Torr fittings equipped with shut-off valves. Both ends of the reactor were sealed with Kapton windows. Samples that required pretreatment prior to XAS measurements were placed in reactors with an internal thermocouple directly touching the sample holder; this thermocouple provided feedback control for the clam-shell furnace used to heat the reactor. The Zn/SiO_2 samples were tested at room temperature after synthesis and under two pretreatment conditions: (1) flowing H_2/He (100 cc/min) at 200 °C, and (2) flowing H_2/propylene/He (100 cc/min) at 200 °C. After sample pretreatment at 200 °C, the XAS measurements were obtained after the catalysts were cooled in He to room temperature without exposure to air. Ionization chambers were optimized at the midpoint of the Zn spectrum for the maximum current with linear response (~10^{10} photons detected s^{-1}) using 5% Ar in N_2 (15% absorption) in the incident X-ray detector and a mixture of ~25% Ar in N_2 (70% absorption) in the transmission X-ray detector. A third detector in the series simultaneously collected a Zn foil reference spectrum with each measurement for energy calibration. A cryogenically cooled double-crystal Si(1 1 1) monochromator was used and detuned to 50% to minimize higher harmonics. The X-ray beam was 0.5 × 1.5 mm, and data were collected in transmission geometry over 10 min in step-scan mode.

The Zn K-edge XANES energy was determined from the inflection point of the leading edge by determination of the energy of the maximum in the first peak of the first derivative. Extended X-ray absorption fine structure (EXAFS) fits of the Zn/silica catalysts were determined from experimental phase shift and backscattering amplitudes using standard procedures within WINXAS 3.1 software. The EXAFS coordination parameters were obtained by least-squares fit in r-space of the first shell nearest neighbor, k^2-weighted Fourier transform data. Zn—O phase and amplitude were obtained from a Würtzite ZnO reference (3 Zn—O bonds at 1.974 Å and 1 Zn—O bond at 1.988 Å): the k^2-weighted Fourier transformed spectrum was reverse-transformed over the range 0.96–2.16 Å to select for first-shell Zn—O scattering, and the resulting phase and amplitude used to define a scattering reference for 4.0 Zn—O bonds at 1.98 Å. Zn—C phase and amplitude were obtained from $ZnEt_2$ (2 Zn—C bonds at 1.95 Å): the k^2-weighted Fourier transformed spectrum was reverse-transformed over the range 0.84–2.04 Å, and the resulting phase and amplitude used to define a scattering reference for 2.0 Zn—C bonds at 1.95 Å. These scattering references were then used to fit Zn—O and Zn—C scattering contributions to samples of interest. Reported $\Delta\sigma^2$ values are defined as $\Delta\sigma^2 = \sigma^2(\text{sample}) - \sigma^2(\text{reference})$, where the value of σ^2(reference) is implicitly contained within the reference phase and amplitude data. A $\Delta\sigma^2$ value near zero indicates that sample and reference have similar values for the pseudo-Debye Waller factor. Absolute values of σ^2 were not determined in general; examination of selected spectra applying FEFF 6.0 calculations within the Artemis software package to experimental crystal structures suggested absolute values for σ^2 of 0.0025 for Zn—C first shell scattering in $ZnEt_2$ and 0.0031 for Zn—O first shell scattering in ZnO. Transfer of experimentally measured backscattering amplitudes from references to samples directly accounts for the energy-dependent variation in scattering amplitude for each scattering path, obviating the need for the S_o^2 correction factor. Examination of selected spectra within Artemis suggested an $S_o^2 = 0.80$ for both Zn—O and Zn—C.

2.6. X-ray diffraction

Crystalline phase compositions of the ALD-synthesized Zn/SiO_2 samples were determined by powder X-ray diffraction using a Bruker Diffractometer D8 Advance operating with the following parameters: Cu Kα radiation of 40 mA, 40 kV, $K_\lambda = 0.15418$ nm, 2θ scanning range of 5–70°, a scan step size of 0.005° and a time of 3 s per step. The samples were ground and placed on a zero background silicon holder (MTI Corp.) for analysis.

2.7. Transmission electron microscopy (TEM)

High resolution TEM images were obtained at the University of Illinois-Chicago's Research Resources Center facility using the JEM-3010 (a 300 kV transmission electron microscope with a LaB_6 electron source). The JEM-3010 is an ultrahigh resolution analytical electron microscope with a point resolution of 0.17 nm. Each sample was dispersed in deionized water and sonicated for 20 min. A drop of the suspension was added to a holey-carbon copper grid and dried under a heat lamp for 10 min. Imaging was performed in bright field mode with an objective aperture selected to permit lattice imaging. A minimum of 100 particles were counted to get an accurate representation of the particle size distribution for each catalyst using Digital Micrograph software.

2.8. Density functional theory computational methods

First-principles calculations based on the hybrid density functional theory (B3LYP) [23] were conducted to simulate the

mechanism of ethyl group activation on zinc under catalytic conditions. The catalyst surface was simulated using cluster models representing silsesquioxane cage structures. Such models have been successfully used in our previous studies [4a]. The structure optimizations and free energy calculations of different reaction intermediates and transition states were performed using the Gaussian-09 quantum chemistry software [24]. The accuracy of the transition state (TS) calculations was verified through intrinsic reaction coordinate (IRC) scans [25] and frequency analysis. TZVP basis sets were used to perform the calculations (B3LYP/TZVP) [26].

3. Results and discussion

3.1. Catalyst synthesis by ALD

Various zinc on silica catalysts were synthesized by ALD using diethylzinc (DEZ) as precursor and, in some cases, water in a subsequent synthesis step (Scheme 1). The self-limiting nature of the gas-phase grafting technique was verified through a series of ZnO deposition experiments under surface saturating conditions. Table 1 summarizes the results of these ALD synthesis experiments on silica pre-dried at 200 °C (4.9 α-OH/nm^2) [19,21]. In this paper, a complete zinc oxide monolayer is defined as the material generated from the reaction of one equivalent of DEZ with one equivalent of surface hydroxyl groups (α-OH). One-cycle ZnO deposition experiments employing total DEZ doses of 0.75 Torr-s and 1.5 Torr-s on 160 mg SiO_2 (0.39 mmol α-OH) afforded Zn_A and Zn_B (Table 1), respectively. ICP-AES analysis of Zn_A and Zn_B revealed identical zinc loadings of 10% (per weight basis; 0.29 mmol). The identical zinc loading despite the difference in total DEZ dosage employed in the ALD synthesis confirms the self-limiting nature of the zinc oxide deposition [27–29]. The self-limiting deposition reaction is also supported by findings from the mass spectrometric monitoring of the reaction between silica and excess amount of DEZ at 100 °C and 175 °C (see Figs. S1–S3 in the Supporting Information).

The observed 10% Zn loading (0.29 mmol Zn) suggests that, during the first ALD half-reaction, silica surface saturation by ethylzinc(II) species constitutes ~75% of a theoretical monolayer (0.39 mmol Zn). This coverage limit is attributed to steric crowding of ethyl-zinc(II) fragments on the silica surface. (Note: The 0.75 Torr-s ALD method for Zn_B is estimated to deliver ~83 mg (0.67 mmol) DEZ. The 0.29 mmol Zn on Zn_B constitutes to 43% of the total Zn pulsed. The rate of DEZ delivery is estimated to be 110 mg (0.89 mmol) DEZ/Torr-s. This number is based on the consumption of 5 g of DEZ over 45 Torr-s.) Analysis of the top and bottom regions of the Zn_B bed revealed Zn loadings of 12% and 10%, respectively, both of which are consistent with submonolayer coverage by Zn species and an ALD-type deposition mechanism. Three successive ZnO cycles gave Zn_C (Table 1) with 27% Zn. This Zn content suggests that, on the average, 19 mg (0.29 mmol) Zn is deposited per ZnO deposition cycle. This result is a demonstration of the reproducibility of the ALD synthesis method.

The zinc oxide-type sites generated from the ALD synthesis were characterized via diffuse-reflectance infrared Fourier-Transform spectroscopy (DRIFTS) and X-ray absorption spectroscopy (XAS), and were found to be isolated tetracoordinate Zn (II) sites on silica (b, Scheme 1). On the other hand, since the product of the first ALD half reaction (a, Eq. (1) in Scheme 1) is air-sensitive and cannot be transported out of the I-ALD tool under inert-atmosphere conditions, spectroscopic characterization of ethyl-zinc on silica was carried out using the product generated from the room-temperature solution grafting of DEZ on silica (Zn_{Et}, Eq. (2), Scheme 1). Spectroscopic characterization of Zn_{Et} (*vide infra*) revealed a tricoordinate configuration for the ethyl-zinc/SiO_2 species. Detailed discussion of the spectroscopic data for both zinc species will be presented in the latter section of this paper.

3.2. Catalytic propylene hydrogenation activity

The catalytic activities of the ALD-synthesized Zn/SiO_2 systems were investigated for propylene hydrogenation and propane dehydrogenation under plug-flow conditions, with the I-ALD-CAT tool in "*catalysis mode*". Each catalyst performance evaluation was carried out immediately after the *in situ* catalyst synthesis by ALD. This feature of the I-ALD-CAT tool allows for systematic comparison of the catalytic reactivity of zinc oxide and alkyl zinc-type active sites without exposure to air and moisture during the course of the experiment. Our group recently reported a single-site Zn/SiO_2 catalyst prepared by strong electrostatic adsorption (SEA) of $[Zn(NH_3)_4]^{2+}$ **Zn_{SEA}** that hydrogenates propylene at 200 °C with the Zn(II) sites functioning as Lewis acid centers that heterolytically activate H—H and C—H bonds under hydrogenation and dehydrogenation conditions, respectively [4a]. Homogeneous and heterogeneous zinc materials that either catalytically or stoichiometrically hydrogenate olefins are rare [31–33,36]. Of the few stoichiometric systems that insert an olefin into a Zn—H bond,

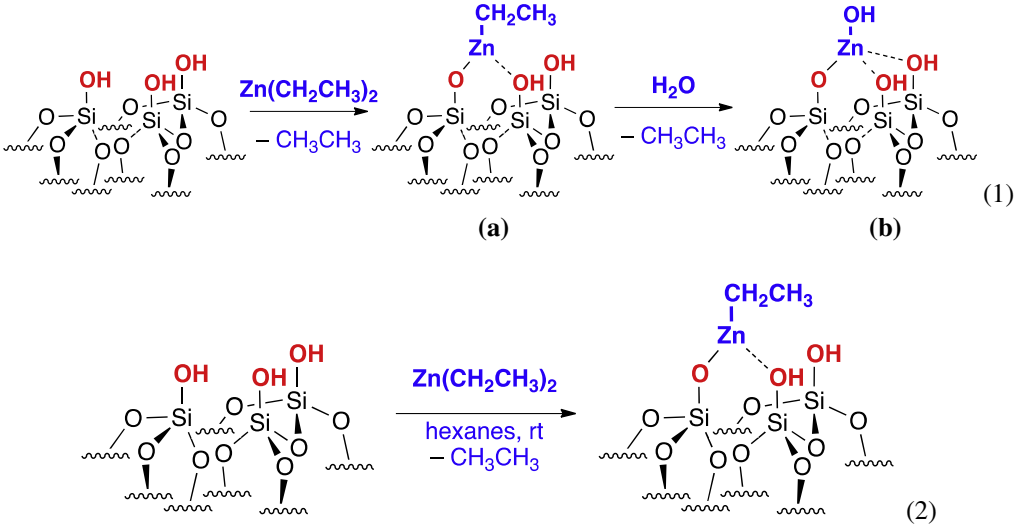

Scheme 1. (1) Synthesis of Zn/SiO_2 via atomic layer deposition at 175 °C. (2) Synthesis of H_3CH_2–Zn/SiO_2 (Zn_{Et}) via solution grafting.

Table 1
Zn/SiO_2 synthesis by atomic layer deposition.

ALD Synthesis Method	ALD Cycle(s)	Temperature (°C)	SiO_2 (mg)	Zn (wt%)	Type of Zn species formed
$\mathbf{Zn_A}$ [1.5 Torr-s DEZ) + (1.5 Torr-s H_2O)]	1	175	160	10	Monodispersed zinc oxide sites (submonolayer)
$\mathbf{Zn_B}$ [(0.75 Torr-s DEZ) + (0.75 Torr-s H_2O)]	1	175	160	10	
$\mathbf{Zn_C}$ [(0.75 Torr-s DEZ) + (0.75 Torr-s H_2O)]	3	175	160	27	Film
$\mathbf{Zn_D}$ [(0.75 Torr-s DEZ) + (0.75 Torr-s H_2O)]	10	175	160	49	
$\mathbf{Zn_E}$ (0.75 Torr-s DEZ)	1	175	160	10	Ethylzinc(II) sites
$\mathbf{Zn_F}$ (0.3 Torr-s DEZ)	1	175	320	2.2	
$\mathbf{Zn_G}$ (0.75 Torr-s DEZ)	1	175	320	4.5	
$\mathbf{Zn_H}$ (0.3 Torr-s DEZ)	1	100	320	3.7	

promoter complexes of Ti or Ni are necessary [36–37]. Zn/ZSM-5, on the other hand, lacks olefin hydrogenation activity since olefin polymerization by the protons in the catalyst framework is more favorable [4a]. Similar to Zn_{SEA}, the ALD-synthesized catalysts required high hydrogenation temperatures (>150 °C; Note: Propylene hydrogenation results presented in this section were obtained at 200 °C) [4a]. The catalysts are 100% selective to propane, with no other hydrocarbon products observed. The SiO_2 support is unreactive under the given conditions while the ALD-synthesized Zn/SiO_2 catalysts exhibit various rates of deactivation as influenced by Zn loading and SiO_2 pretreatment conditions. Interestingly, the ALD catalyst synthesis methods that involve water treatment of the ethyl zinc submonolayer on SiO_2 generate unstable, low-reactivity materials. For example, a submonolayer of monodispersed ZnO on SiO_2 ($\mathbf{Zn_B}$), hydrogenates propylene but deactivates completely in the first 30 min of the reaction. The low activity and stability of Zn_B is attributed to the facile agglomeration of the Zn sites, forming ZnO clusters which are inactive for hydrogenation under the given conditions [30–35]. This is consistent with TEM images of Zn_B which show the presence of ~20 nm ZnO particles (a, Fig. 3). This mode of ZnO speciation is consistent with reported island-like nucleation of ZnO on oxide supports [30]. Our work shows that the formation of island-nuclei appears to occur during the water pulse, with the initial ethyl-zinc surface species being well-dispersed. Conformal ZnO sub-monolayer deposition cannot be completely ruled out since the observed particles may have formed upon exposure to the atmosphere prior to TEM imaging. Moreover, varying degrees of particle formation were also observed in several spent Zn/SiO_2 catalysts (*vide infra*) further confirming the mobility of Zn(II) sites on the silica surface.

The propylene hydrogenation activity of ethyl zinc sites on silica was also evaluated. Zn_E, with Zn loading identical to Zn_B (Table 1), is catalytically inactive at room temperature and exhibits

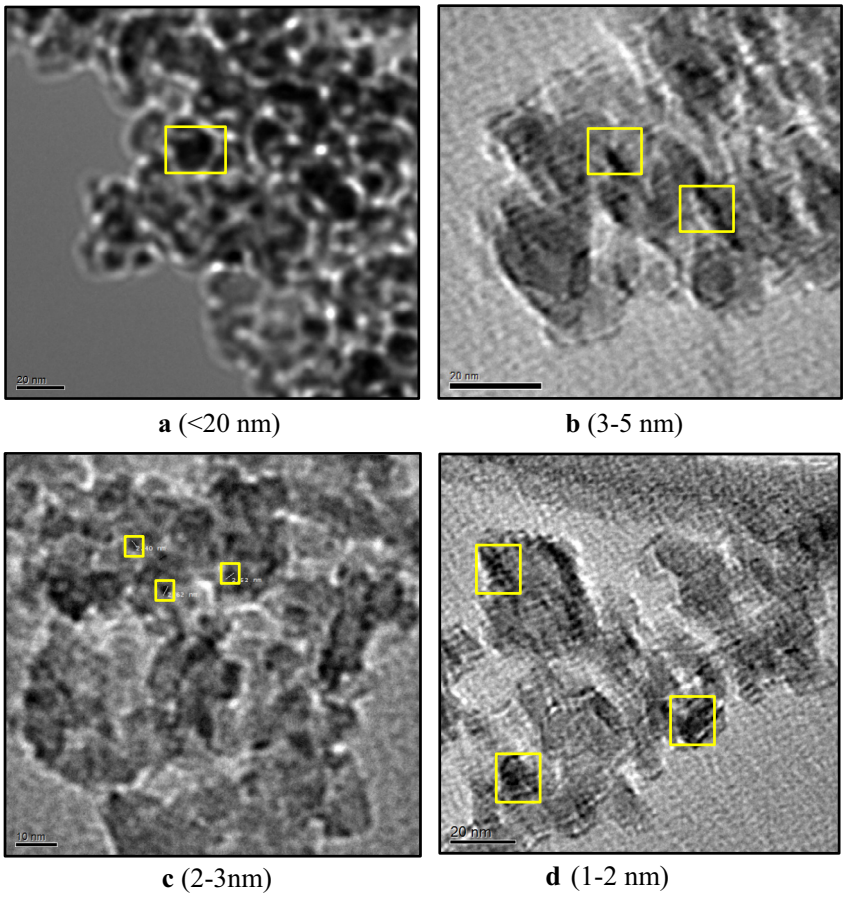

a (<20 nm) **b** (3-5 nm)

c (2-3nm) **d** (1-2 nm)

Fig. 3. Bright Field TEM images of Zn/SiO_2 synthesized by ALD. (a) Zn_B, (b) Zn_E (spent), (c) Zn_F (spent) and (d) Zn_G (spent).

hydrogenation activity above 150 °C. Zn_E hydrogenates propylene at 200 °C (TOF_{0h} = 0.159 h^{-1}, TOF_{3h} = 0.012 h^{-1}; Fig. 4); however, it completely deactivates in ~3 h due to Zn agglomeration (3–5 nm particles; **b**, Fig. 3). Notably, Zn_E exhibits higher initial hydrogenation activity compared to Zn_B. The observed disparity in the *initial hydrogenation activities* (t < 80 min) between these Zn/SiO_2 with identical Zn loadings (~75% of a monolayer) is attributed to differences in the precatalyst structure: One-cycle DEZ–H_2O experiment generates Zn_B with closed shell 18-electron, tetracoordinate Zn(II) centers. The higher initial activity of Zn_E, on the other hand, is expected for the open-shell 16-electron, tricoordinate ethyl zinc(II) sites present. These open-shell Zn(II) sites are expected to exhibit enhanced substrate binding affinity while the zinc–ethyl functionality is a reactive site that can heterolytically activate hydrogen (*vide infra*). In contrast to Zn_B, Zn_{SEA} and bulk ZnO, catalyst Zn_E *does not require high-temperature pretreatment conditions*, consistent with the higher reactivity for supported alkyl zinc species under similar conditions. Overall, the hydrogenation activity of Zn_E confirms that supported alkyl zinc species provide a convenient entry into the catalytic cycle.

The observed facile deactivation of Zn_B and Zn_E suggests that *Zn (II) isolation is the key factor to access stable catalysts.* Hence, optimization of ALD synthesis conditions (e.g. substrate preparation, DEZ dose) was conducted to increase active site dispersion and, in turn, produce catalysts with improved activity and stability. Reducing the DEZ dosing time from 0.75 Torr-s to 0.3 Torr-s and doubling the substrate loading (320 mg) afforded catalyst Zn_F (2.2% Zn; Table 1) with increased activity (TOF_{0h} = 0.650 h^{-1}, TOF_{12h} = 0.280 h^{-1}, Fig. 4) and longer catalyst life. Zn_F deactivates, retaining only 31% of its initial activity after a 12-h reaction period. TEM imaging of spent catalyst Zn_F revealed the formation of smaller ZnO particles (2 nm; **c** in Fig. 3), indicative of slower agglomeration and retained monodispersity of majority of the Zn(II) sites. The single-site nature of majority of the Zn sites in catalyst Zn_F post-catalysis is confirmed by EXAFS data where second-shell scattering due to sintered Zn sites were not observed.

Silica dehydration *in vacuo* at 600 °C to reduce surface hydroxyl concentration also resulted in improved organo-zinc site dispersion. A 0.75 Torr-s DEZ deposition on 320 mg $SiO_{2-600°C}$ generates catalyst Zn_G (4.5% Zn, Table 1) with improved hydrogenation activity compared to Zn_E (TOF_{0h} = 0.318 h^{-1}, TOF_{12h} = 0.137 h^{-1}). Zn_G exhibits improved stability, retaining 42% of the initial activity after 12 h of testing (Fig. 7). Post-catalysis images of Zn_G support improved Zn dispersion based on the smaller particles observed (1–2 nm; **d** in Fig. 3).

The effect of the deposition temperature on catalytic reactivity was also explored. 0.3 Torr-s DEZ was grafted at 100 °C, affording Zn_H (Table 1) with 3.7% Zn (wt). The resulting material exhibits lower hydrogenation activity (TOF_{0h} = 0.393 h^{-1}, TOF_{0h} = 0.167 - h^{-1}) relative to Zn_F (2.2% Zn), which was synthesized at 175 °C. The observed lower zinc deposition at 175 °C suggests that self-decomposition of DEZ that can lead to CVD is *not a major factor during the one-cycle Zn deposition experiments* employed in this study. An earlier report by Weimer and coworkers suggests that DEZ-H_2O at 177 °C resulted in variations in Zn loading due to DEZ self-decomposition at high temperatures [38]. However, they also emphasized that self-decomposition only becomes a challenge under conditions where overexposure of DEZ to decomposing temperatures (e.g., 10 cycle DEZ-H_2O deposition or more) occurs [38]. The higher zinc loading (3.7%) at a lower temperature (100 °C) is attributable to higher surface hydroxyl concentration on the silica substrate resulting in the formation of catalytically inactive zinc clusters. This aspect presents the advantage of high-temperature, gas-phase organometallic grafting for the nucleation of single-atom sites over traditional liquid- and gas-phase techniques under ambient conditions; *isolated catalytic sites can be grafted under conditions that allow for thermal control of surface hydroxyl concentrations.* Reference catalyst Zn_{SEA}, with Zn loading similar to Zn_H (4% Zn), shows lower activity under the given conditions (TOF_{0h} = 0.107 h^{-1}, TOF_{12h} = 0.043 h^{-1}) Note: Due to instrument

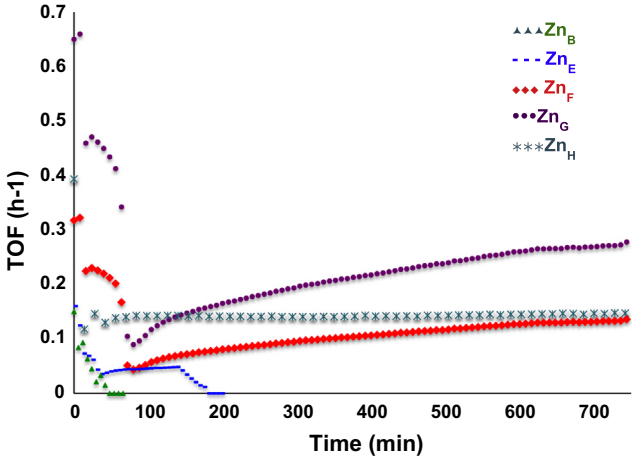

Fig. 4. Hydrogenation of propylene reactivity of Zn_B, Zn_E, Zn_F, Zn_G and Zn_H at 200 °C. The apparent TOF was calculated based on the total amount of Zn present in the catalyst.

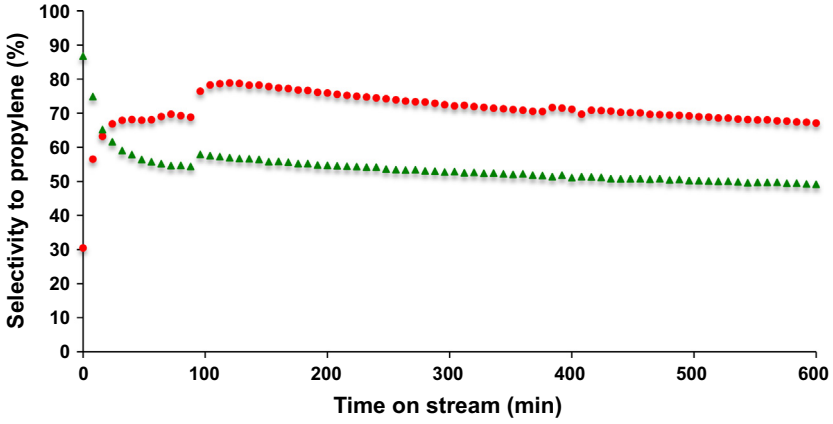

Fig. 5. Dehydrogenation selectivity of Zn_F (red circles) and Zn_{SEA} (green triangles) to propylene. The calculated TOF was calculated based on the total amount of Zn present in the catalyst.

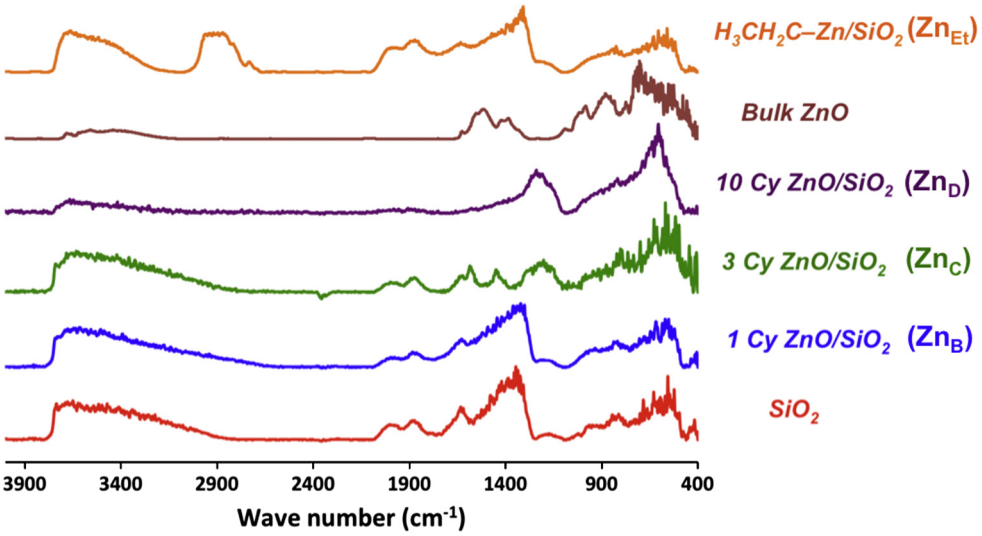

Fig. 6. Infrared spectra of SiO_2 (red), Zn_A (blue), Zn_C (green), Zn_D (purple), bulk ZnO (brown) and Zn_{Et} (orange).

design limitations, the conditions employed in the previously reported Zn_{SEA}-catalyzed hydrogenation study [4a] cannot be implemented in the present study. Slower flow rates were employed in the catalysis experiments. The slower Zn_{SEA} hydrogenation rates reported in this study are due to a shorter contact time employed (1.3 s); This is almost half of that employed in our previous report (~2.0 s) [4a].

Interestingly, the period where higher initial activity with catalysts $Zn_{E\text{-}H}$ was observed (t < 80 min) coincides with active generation of C_2 and C_4 hydrocarbons, further confirming that supported alkyl zinc species provide reasonable entry into the catalytic hydrogenation cycle. Notably, systems with increased Zn dispersity ($Zn_{F\text{-}G}$) exhibit long-term activity (t > 12 h) with Zn_F and Zn_G exhibiting enhanced activity over time. This is an indication of the dynamic nature of these surface sites under reaction conditions, however, no definitive explanation can be offered yet for this phenomenon.

3.3. Catalytic propane dehydrogenation activity

Catalytic propane dehydrogenation activity was determined at 550 °C as equilibrium conversion is reasonable (~30%), while thermal cracking contributions at this temperature are minimal [4a]. Both zinc oxide- and ethylzinc(II)-saturated SiO_2 catalysts (Zn_B and Zn_E, respectively) are inactive for propane dehydrogenation at 550 °C. The lack of activity is attributable to Zn sintering to ZnO clusters that are known to be inactive for propane dehydrogenation [39]. The more dispersed ethylzinc(II) sites in Zn_F, on the other hand, selectively catalyzes propane dehydrogenation (TOF_{0h} = 0.103 h^{-1}, TOF_{12h} = 0.042 h^{-1}; Fig. 5) over a 12 h period. Since the study aims to differentiate the dehydrogenation activity of ZnO (e.g., Zn_{SEA}) and ethyl-zinc-type sites (Zn_F), catalyst Zn_F was tested for propane dehydrogenation immediately after the ALD synthesis without the pre-activation with H_2 step implemented for Zn_{SEA}. Lower selectivities for propylene (30–70%) were observed for Zn_F in the first ~90 min of testing since this period coincides with the generation of ethane and ethylene from the activation of the ethyl-zinc/SiO_2 precatalyst. At t > 90 min, higher selectivities to propylene (78% selectivity to propylene) were observed; however, propylene selectivity decreases to 65% by the end of the 12 h reaction period. Under identical conditions, Zn_{SEA} exhibits lower activity (TOF_{0h} = 0.071 h^{-1}, TOF_{12h} = 0.020 h^{-1}) and propylene selectivity (Fig. 5).

The dehydrogenation reaction also produces ethylene, methane and butane, which are products of competing C—C bond activation pathways. The Zn/SiO_2 catalyst dehydrogenation selectivity originates from the preference of these Lewis acidic centers for primarily activating C—H bonds over C—C bonds [4a]. The observed catalyst selectivity for C—H bond activation is consistent with the greater propensity of Zn(II) propyl species to undergo β-hydrogen elimination over β-methyl elimination. The energy of activation for the former pathway (C—H bond activation) is ~10 kcal lower than the energy barrier for the latter process (C—C bond scission) [4a,40]. The activation of catalyst Zn_F can proceed through protonation of the zinc-ethyl functionality by adjacent surface hydroxyls, producing ethane and a three-coordinate Zn(II) active site – the proposed active site in Zn_{SEA} (see Fig. 11, vide infra).

3.4. Infrared spectroscopy

Fig. 6 shows the infrared spectra of the Zn/SiO_2 catalysts prepared by ALD and solution grafting methods. One-cycle ZnO deposition on SiO_2 affords materials (e.g., Zn_B) that exhibit infrared spectral features identical to that of the silica substrate [41]. The spectra of SiO_2 and Zn_B show strong, broad absorptions at 3700 cm^{-1} to 2900 cm^{-1} (Si—OH stretching), 1650 cm^{-1} (H_2O adsorbed by siliceous materials), and 1250 cm^{-1} (Si—O bond stretching). The deposition of three and ten cycles of ZnO produces Zn_C and Zn_D (10 ZnO cycles; 0.75 s DEZ–0.75 s H_2O) that exhibit shifted Si—O absorption in the 1200 cm^{-1} region. Zn_C, Zn_D and bulk ZnO exhibit weak O—H stretching bands (3700 cm^{-1} to 2900 cm^{-1}) [42], potentially indicative of lower O—H concentration. On the other hand, the spectrum of Zn_{Et} (solution grafting) shows strong absorption at 2900 cm^{-1} which is attributable to C(sp^3)—H bond stretching, confirming the presence of zinc-bound ethyl functionality after the solution-phase grafting.

3.5. Multinuclear (^1H, ^{13}C, ^{29}Si) Solid-state MAS NMR spectroscopy

Fig. 7a shows the solid-state ^1H MAS NMR spectra of the Zn_{Et}, Zn_B and non-metalated silica substrate. The upfield chemical shift at 0.31 ppm for **Zn_{Et}** is indicative of zinc-bound methylene protons (*Zn—CH_2*) based on reported solution-phase ^1H-NMR spectral data for DEZ with the Zn—*CH_2*—CH_3 chemical shift at 0.30 ppm [43]. The Zn—*CH_2* chemical shift overlaps with a broad signal ranging from 3 to −1 ppm, and with peak at 0.79 ppm. This broad peak could arise

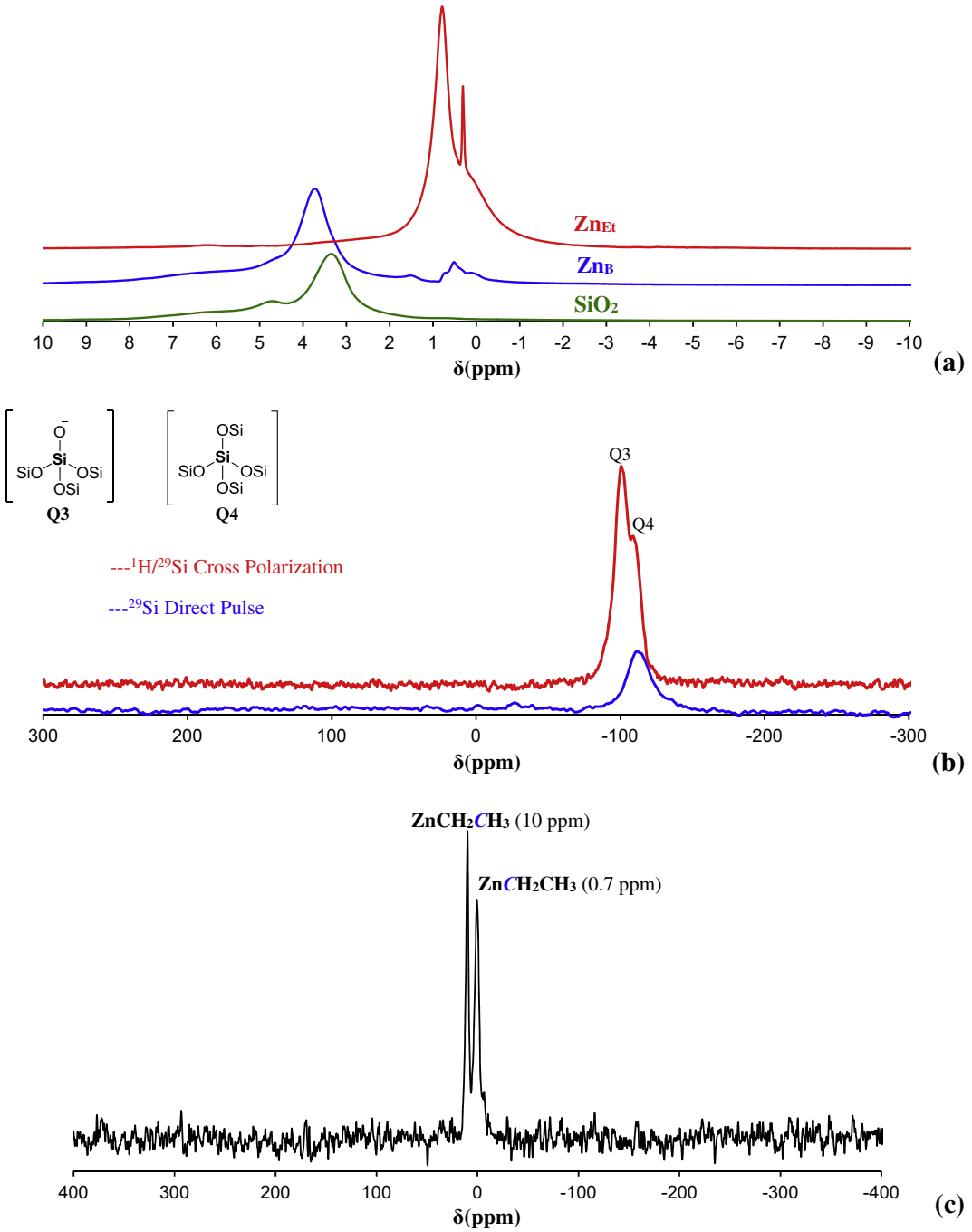

Fig. 7. (a) Solid-state ^{1}H MAS NMR spectra of $\mathbf{Zn_{Et}}$ (green), $\mathbf{Zn_B}$ (red), and $\mathbf{SiO_2}$ (blue); (b) ^{29}Si direct pulse and ^{1}H/^{29}Si cross polarization MAS NMR spectrum of Zn_{Et}; and (**c**) ^{13}C MAS NMR spectrum of Zn_{Et}.

from the terminal methyl protons of Zn—CH_2—CH_3, Si—OH, Si—OCH_2CH_3 and Si—CH_2CH_3 groups [44]. The absence of Si***C***H_2CH_3 groups in Zn_{Et} is further confirmed by direct-pulse [29] Si and cross-polarization ^{1}H ^{29}Si MAS NMR experiments where only chemical shifts in the −100 to −115 ppm range, corresponding to tetrahedral Si centers typically observed in mesoporous silica materials, were observed (Fig. 7b). ^{13}C MAS NMR experiments on Zn_{Et} (Fig. 7c) show only two chemical shifts occurring at 0.7 (Zn—CH_2) and 10 ppm ($ZnCH_2$***C***H_3), confirming the presence of zinc-bound ethyl groups. The absence of downfield ^{13}C chemical shifts expected for silyl ethers and upfield signals for silanes (e.g., Si***C***H_2CH_3) is indicative of the absence of Si—O—***C***H_2CH_3 and Si***C***H_2CH_3 groups.

One-cycle DEZ deposition under surface-saturating conditions (0.75 Torr-s) followed by water treatment affords Zn_B (10% Zn, w/w). Zn_B shows a major proton chemical shift at 7 to 2 ppm (silica O—H functionalities, Fig. 7a). Interestingly, the broad chemical shifts from 0.8 to 0 ppm were observed at a lower intensity, indicating that the intense chemical shifts in the Zn_{Et} spectrum could be mainly due to zinc-bound ethyl groups that can undergo protonolysis upon water treatment. Elemental analysis of $\mathbf{Zn_{Et}}$ revealed 10.5% Zn loading (0.16 mmol) and 3.5 wt% C (0.29 mmol). The corresponding molar composition translates to a 1.1:1.0 Zn-to-ethyl group ratio. Under the assumption that no unreacted DEZ is present in Zn_{Et}, this ratio indicates that 91% of all Zn sites have metal-bound ethyl groups, while the remaining 9% underwent

complete protonolysis of the two Zn—C bonds to form ZnO-type centers.

3.6. X-ray absorption spectroscopy (XAS) and powder X-ray diffraction (PXRD)

X-ray absorption spectroscopy (XAS) was employed to elucidate the zinc oxidation state and coordination environment in the Zn/SiO_2 systems. The X-ray absorption near edge spectra (XANES) and Extended X-ray Absorption Fine Structure (EXAFS) are considered separately. XANES is sensitive to both coordination number (CN) and the electronegativities of the nearest neighbors around Zn(II): absorption edge energies shift to higher energies with larger CN, greater nearest neighbor electronegativity, and higher formal oxidation state of the absorbing atom, while post-edge features (EXAFS) provide an additional structural fingerprint. EXAFS provides information about the number of, and distance to, near neighbors of the scattering atom.

XAS characterization of Zn_{Et} (DEZ solution grafting) and Zn_B (one-cycle ZnO deposition) was carried out to elucidate the nature of the Zn sites generated from the two ALD half reactions: (1) DEZ grafting and (2) the subsequent H_2O treatment step. The latter is discussed first. The XANES spectrum of Zn_B closely resembles that of a single site Zn^{2+}/SiO_2 catalyst previously reported by our group (Zn_{SEA}), suggesting similar coordination environments around Zn in both materials (Fig. 8). The edge energies for these materials are 9.6644 keV and 9.6646 keV respectively, slightly greater than the 9.6637 keV edge energy of the Würtzite ZnO standard and consistent with four-coordinate, divalent Zn. However, the relative intensities of the first two absorption maxima above the edge in Zn_{SEA} and Zn_B differ from those of ZnO, supporting the conclusion that the Zn in these samples is not located in Würtzite-structured domains. While precise assignment of XANES absorption features is in general not possible without high level electronic structure theory calculations, the absorption spectrum of ZnO roughly mirrors the conduction band density of states in this well-studied semiconductor, while the pair of absorption maxima for Zn_{SEA} and Zn_B can reasonably be assigned to Zn 4p-derived states of A_1 (p_z) and E (p_x,p_y) symmetry for single site $Zn(OSi)_2(HOSi)_2$ centers of approximate C_{2V} symmetry [4a].

As in ZnO, zinc in DEZ is also formally divalent. However, the lower electronegativity of carbon vs. oxygen and the two-coordinate linear geometry in DEZ give rise to significant differences between their XANES spectra. In particular, the edge energy of 9.6618 keV is closer to that of Zn metal foil (9.6608 keV) than to that of ZnO. However, the maximum absorption in the DEZ spectrum at 9.6625 keV makes DEZ readily distinguishable from Zn metal, which lacks this feature. In DEZ, the strong absorption at the XANES edge is a result of the allowed photoexcitation of a Zn 1 s electron into the two unoccupied, nonbonding Zn 4p orbitals provided by the linear coordination geometry. The third Zn 4p orbital in DEZ is of $\sigma*$(Zn—C) character and its energy is well above the ionization energy for the Zn 1 s electron; the resulting short lifetime of this state gives rise to a broad, low intensity feature near 9.675 keV.

The value of the edge energy for Zn_{Et} (9.6624 keV) is intermediate between that of ZnO (9.6637 keV) and DEZ (9.6618 keV), consistent with a bonding environment intermediate between these references. The first absorption maximum above the edge is of lower intensity than that of DEZ and more comparable to that of ZnO, suggesting smaller contribution from nonbonding Zn 4p orbitals and therefore a coordination number greater than 2. This interpretation is supported by a fit to the EXAFS region of Zn_{Et}, which yields CN ≈ 3. While the edge energy of 9.6624 keV is lower than that of ZnO, it is greater than that of DEZ and remains consistent with Zn in the 2+ oxidation state. A detailed investigation into the effects of coordination number, ligand electronegativity, and ligand-metal bond character in gallium organometallic compounds and dehydrogenation catalysts has recently been reported by our group [49].

Fig. 9 shows the extended X-ray absorption fine structure (EXAFS) spectra recorded for Zn_{Et} and Zn_B, and the Zn(II) standards DEZ and ZnO. DEZ is monomeric both in solution [45] and in the solid phase [46], with the two-coordinate Zn center exhibiting an average Zn—C bond distance of 1.95 Å. DEZ exhibits a relatively small first shell Zn—C scattering centered near 1.4 Å (phase-uncorrected distance) and no meaningful higher shell scattering. Bulk zinc oxide, on the other hand, adopts the Würtzite structure with each four-coordinate Zn(II) center surrounded by four oxygen atoms in a nearly tetrahedral environment (average Zn—O bond distance of 1.98 Å) [4a,47]. ZnO exhibits a more intense first shell scattering centered near 1.5 Å (phase uncorrected distance). The observed greater intensity of the first shell scattering peak for ZnO compared to DEZ results from differences in (1) Zn coordination numbers (ZnO = 4; DEZ = 2) and (2) intrinsic scattering amplitude of the zinc-bound atoms (O scattering > C scattering).

The first shell scattering peak intensity for Zn_{Et} is consistent with tri-coordinate Zn(II) centers; each 16-electron Zn center is bound to two O atoms and one C atom (average bond distance of 1.95 Å). No significant higher shell scattering was observed for Zn_{Et}, confirming the uniformity of ethyl zinc(II) species on silica. Zn_B, on the other hand, exhibits first shell scattering with amplitude almost equal to that of ZnO, consistent with the presence of 18-electron, four-coordinate Zn(II) sites with a 1.97 Å average Zn—O bond distance [4a]. Zn_B exhibits a very weak second-shell

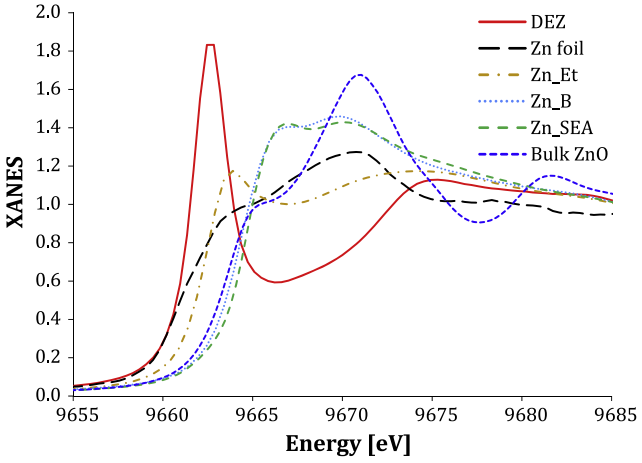

Fig. 8. XANES spectra of DEZ, Zn foil, Zn_{Et}, Zn_B, and bulk ZnO.

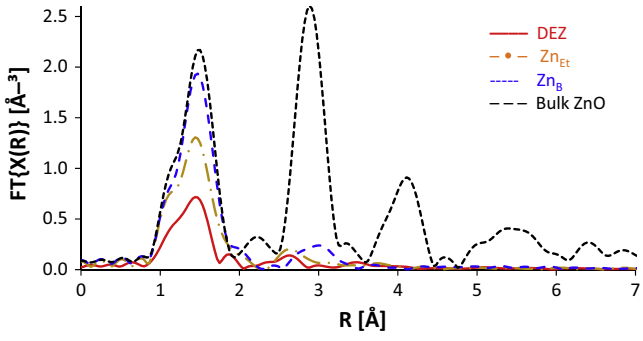

Fig. 9. EXAFS spectra of DEZ, Zn_{Et}, Zn_B and ZnO.

scattering peak and no significant higher shell scattering, indicative of isolated ZnO species. In addition, the XAS spectrum of Zn_B resembles that of the single-site Zn (II) on silica catalyst that we reported earlier, prepared via strong electrostatic adsorption of $[Zn(NH_3)_4]^{2+}$ on silica followed by calcination (Zn_{SEA}, Table 2). The $\Delta\sigma^2$ values for Zn_B and Zn_{SEA} are somewhat greater than zero (i.e. somewhat greater than those of ZnO), consistent with the greater diversity of Zn—O—Si geometries likely to exist on the surface of amorphous silica vs. the crystallographically well-defined Zn—O—Zn environment in ZnO. The unusually large $\Delta\sigma^2$ value for Zn_{Et} may also reflect differences between Zn—O and Zn—C bond lengths; however, attempts to fit Zn—O and Zn—C contributions separately in a single scattering shell lead to mathematically overspecified fits with no unique solutions [4a] Furthermore, ZnO as isolated species in Zn_B is also supported, albeit inconclusively, by the absence of higher nuclearity crystalline phases based on PXRD characterization (Fig. S8 in the Supporting Information (SI)). The PXRD spectrum of Zn_B resembles that of the amorphous SiO_2 support.

Table 2
Summary of XAS data for Zn/SiO_2 species and reference compounds.

Treatment	Edge energy, keV	$N_{Zn-O/C}$	R, Å	$\Delta\sigma^2$ ($\times10^3$)	E_0, eV
ZnO standard	9.6637	4.0	1.98	0.0	−0.1
DEZ standard	9.6618	2.0	1.95	0.0	0.3
H_3CH_2C–Zn/SiO_2 (Zn_{Et})	9.6624	2.9	1.95	5.9	1.1
ZnO (1 cy)/SiO_2 (Zn_B)	9.6644	3.9	1.97	2.3	−2.0
$Zn(NH_3)^{+2}/SiO_2$ Calcined 300 °C (Zn_{SEA})	9.6646	3.8	1.98	2.5	0.2

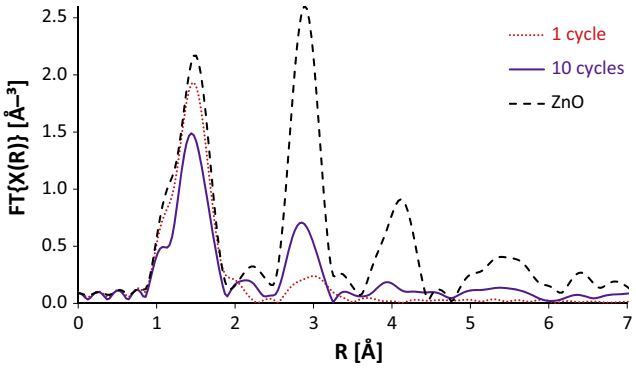

Fig. 10. EXAFS spectra of bulk ZnO, Zn_B (1 cycle ZnO/SiO_2) and Zn_D (10 cycles ZnO/SiO_2).

The EXAFS spectrum of Zn_D (10-cycle deposition of ZnO) features stronger scattering near 3.0 Å and hints of higher shell peaks near 4.0 Å and 5.5 Å (Fig. 10). These higher shell scattering peaks are indicative of higher nuclearity Zn assemblies (e.g., clusters, particles) with structural features similar to bulk ZnO [47,48]. Interestingly, the first shell scattering peak is much weaker in Zn_D, with an average coordination number of 2.7 and bond distance of 1.96 Å. The lower apparent Zn—O coordination number is attributable to the presence of interstitial metallic zinc, also detected by PXRD analysis (Fig. S7b in SI). PXRD analysis of Zn_C (3 ZnO cycles/SiO_2) and Zn_D (10 ZnO cycles/SiO_2) revealed the presence of Zn(0) based on the peaks at $2\theta = 36.3°$, 39.0°, 43.2° and 54.3°.

3.7. Mechanism of Zn—CH_2CH_3 activation

Since the active sites in catalysts $Zn_{E\text{-}G}$ contain ethyl zinc functionalities, the transformations of the ethyl group can be unambiguously monitored, as the incoming substrate (propylene) and hydrogenation product (propane) are both C_3-hydrocarbons. Gas chromatographic monitoring of the C_2 (ethane and ethene) and C_4 (butane) hydrocarbon generated under reaction conditions suggests multiple ethyl-zinc activation pathways. In order to understand the mechanisms of ethyl-zinc activation, Density Functional Theory (DFT) calculations were performed (Fig. 11). Two contributing non-redox pathways are predicted for the observed rapid generation of ethane, which include (1) protonation of the zinc-bound ethyl groups (**2-TS**) by adjacent surface hydroxyls with an intrinsic energy barrier of 35.9 kcal/mol, and (2) direct hydrogenolysis of the Zn—Et bond by molecular hydrogen (**3-TS**) with an intrinsic energy barrier of 57.5 kcal/mol, suggesting that pathway 2 is relatively less favorable. The proposed ethane-generating zinc-ethyl activation pathways are considered *productive organometallic transformations* as they both generate Zn(II) species that are proposed key intermediates in the catalytic cycle. Protonation of the zinc-carbon bond by adjacent surface

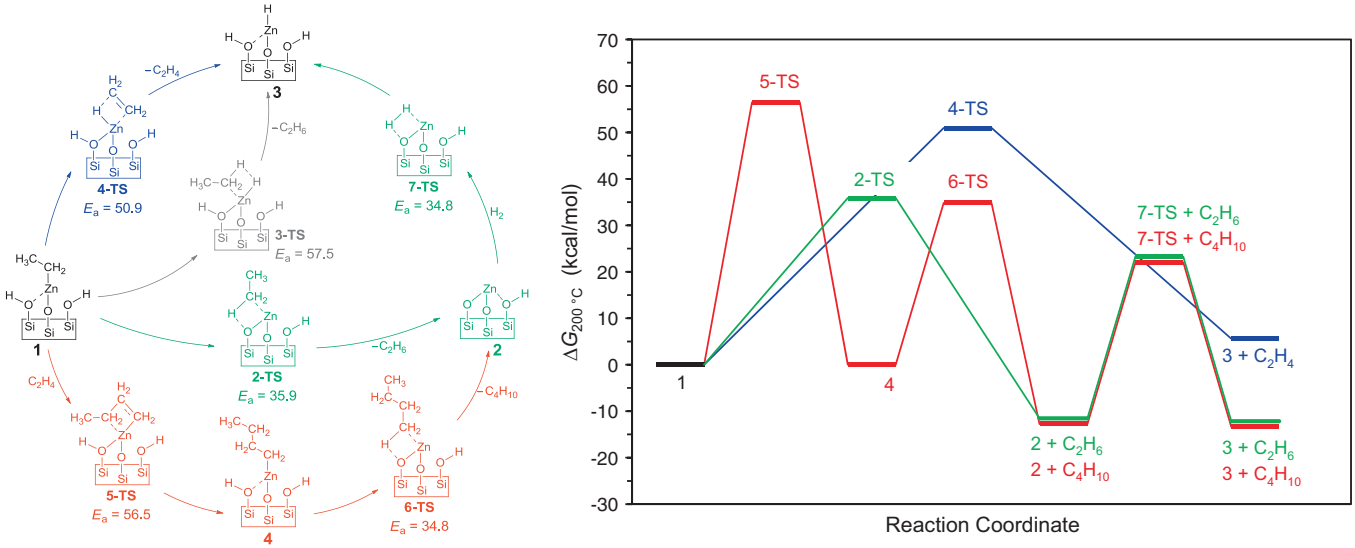

Fig. 11. Different activation mechanisms of Zn—CH_2CH_3 to form C_2 and C_4 hydrocarbons predicted by DFT calculations. The intrinsic activation energy (E_a, kcal/mol) associated with each step is shown.

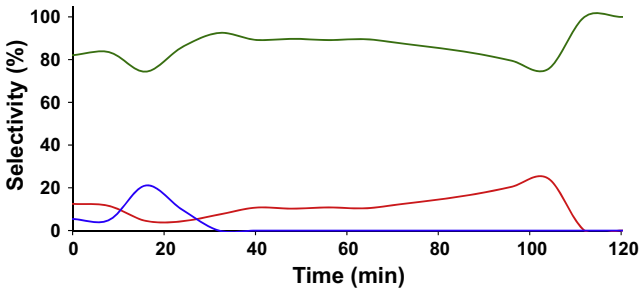

Fig. 12. Plot of H_3CH_2C–Zn activation selectivity to ethane (green), ethylene (red), butane (blue).

hydroxyls forms a three-coordinate 16e^- Zn(II) center (**2**) which is the same active site proposed to be responsible for propane dehydrogenation activity of Zn_{SEA} [4a]. Zn—Et bond hydrogenolysis, on the other hand, generates ethane and a 16e^- Zn(II) hydride (**3**), which was proposed to be a key intermediate in the hydrogenation of propylene by Zn_{SEA} [4a].

The slower generation of ethylene under reaction conditions is consistent with the resistance of zinc alkyl species to β-hydrogen elimination (Fig. 11; **4-TS**, E_a = 50.9 kcal/mol). In addition to ethylene, this pathway also generates a three-coordinate 16e^- Zn(II) hydride (**3**). Butane formation, on the other hand, presumably proceeds via non-reductive route; ethylene generated *in situ* can insert into a Zn—CH_2CH_3 group (Fig. 11; **5-TS**, E_a(calc) = 56.5 kcal/mol), followed by protonation of the resulting zinc-bound butyl group. Activation of the catalyst Zn_E generates ethane, ethylene and butane in a 13:2:1 ratio within the first 20 min of exposure to hydrogen and propylene at 200 °C (Fig. 12). The observed selectivity to ethane, ethylene and butane is consistent with the calculated activation energies at 200 °C for the non-redox ethyl zinc activation pathways discussed above i.e., $E_{a\mathbf{2\text{-}TS}}$ (alkyl protonation) > $E_{a\mathbf{4\text{-}TS}}$ (alkyl protonation) > lc$E_{a\mathbf{5\text{-}TS}}$ (ethylene insertion).

Alternatively, butane formation could proceed through homolytic activation of the ethyl-zinc groups, generating ethyl radicals than can eventually recombine to produce butane, and lower oxidation state zinc species such as metallic zinc. Interestingly, hydrogen activation of the ALD-synthesized catalysts with improved active site dispersion (Zn_F and Zn_G) gives ethane as the main activation product. This supports the hypothesis that higher ethyl zinc loading favors the formation of neighboring zinc alkyl sites that are prone to reductive decomposition and zinc agglomeration.

4. Summary and conclusions

Controlled gas-phase grafting of zinc oxide and organo zinc active sites on high-surface-area silica was achieved using an integrated atomic layer deposition-catalysis (I-ALD-CAT) tool. This approach has provided key insights into the mechanism of zinc grafting on silica supports at the monolayer level, and the reactivity and stability of these Zn sites as a function of dispersion. The I-ALD tool design allowed for the systematic reactivity comparison of different ALD-grafted zinc sites; *in situ* catalysis experiments confirmed much higher reactivity for the open shell 16-electron, tri-coordinate ethyl zinc-silica sites compared to 18-electron, tetra-coordinate zinc oxide-type centers. However, silica surface saturation with Zn(II) sites (~75% of a monolayer) results in facile zinc agglomeration and catalyst deactivation under catalysis conditions. Improved active site dispersion was achieved through reduced DEZ dosing and substrate pretreatment (e.g., dehydration under vacuum), producing Zn/SiO_2 catalysts that are active and stable under propylene hydrogenation (200 °C) and propane dehydrogenation (550 °C) conditions.

Notes

The authors declare no competing financial interest.

Acknowledgments

The work at Argonne National Laboratory was supported by the U.S. Department of Energy (DOE), Office of Basic Energy Sciences, Division of Chemical Sciences, Biosciences and Geosciences. Use of the Advanced Photon Source is supported by the U.S. Department of Energy, Office of Science, and Office of the Basic Energy Sciences, under Contract DE-AC-02-06CH11357. MRCAT operations are supported by the Department of Energy and the MRCAT member institutions. High Resolution TEM images were obtained at UIC's Research Resources Center facility using the JEM-3010. The DFT calculations were performed using the computational resources available at the Argonne National Laboratory Center for Nanoscale Materials (CNM) and the computing resources provided on Fusion and Blues, high-performance computing clusters operated by the Laboratory Computing Resource Center at Argonne National Laboratory.

Appendix A. Supplementary material

Supplementary data associated with this article can be found, in the online version, at http://dx.doi.org/10.1016/j.jcat.2016.10.017.

References

[1] J. Thomas, R. Raja, D. Lewis, Angew. Chem. Int. Ed. Engl. 44 (2005) 6456–6482.
[2] M. McKittrick, C. Jones, J. Am. Chem. Soc. 126 (2004) 3052–3053.
[3] B. O'Neill, D. Jackson, J. Lee, C. Canlas, P. Stair, C.L. Marshall, J. Elam, T. Kuech, J. Dumesic, G.W. Huber, ACS Catal. 5 (2015) 1804–1825.
[4] (a) N. Schweitzer, B. Hu, U. Das, H. Kim, J. Greeley, L. Curtiss, P. Stair, J. Miller, A. Hock, ACS Catal. 4 (2014) 1091–1098;
(b) B. Hu, A. Getsoian, N. Schweitzer, U. Das, H. Kim, J. Niklas, O. Poluektov, L. Curtiss, P. Stair, J. Miller, A. Hock, J. Catal. 322 (2015) 24–37;
(c) V. Dal Santo, M. Guidotti, R. Psaro, L. Marchese, F. Carniato, C. Bisio, Proc. R. Soc. A – Math. Phys. 468 (2012) 1904–1926;
(d) V. Vidal, A. Theolier, J. Thivollecazat, J. Basset, J. Corker, J. Am. Chem. Soc. 118 (1996) 4595–4602;
(e) J. Basset, C. Coperet, D. Soulivong, M. Taoufik, J. Cazat, Acc. Chem. Res. 43 (2010) 323–334;
(f) V. Dufaud, G. Niccolai, J. Thivollecazat, J. Basset, J. Am. Chem. Soc. 117 (1995) 4288–4294;
(g) L. Williams, N. Guo, A. Motta, M. Delferro, I. Fragala, J. Miller, T. Marks, Proc. Natl. Acad. Sci. USA 110 (2013) 413–418;
(h) D. Ruddy, N. Ohler, A. Bell, T. Tilley, J. Catal. 238 (2006) 277–285;
(i) C. Coperet, M. Chabanas, R. Saint-Arroman, J. Basset, Angew. Chem. Int. Ed. 42 (2003) 156–181;
(j) D. Gajan, C. Coperet, New J. Chem. 35 (2011) 2403–2408;
(k) C. Coperet, Chem. Rev. 110 (2010) 656–680.
[5] T. Aaltonen, M. Ritala, Y.-L. Tung, Y. Chi, K. Arstila, K. Meinander, M. Leskelä, J. Mater. Res. 19 (2004) 3353–3358.
[6] H. Feng, J. Lu, P. Stair, J. Elam, Catal. Lett. 141 (2011) 512–517.
[7] B. O'Neill, D. Jackson, A. Crisci, C. Farberow, F. Shi, A. Alba-Rubio, J. Lu, P. Dietrich, X. Gu, C. Marshall, P. Stair, J. Elam, J. Miller, F. Ribeiro, P. Voyles, J. Greeley, M. Mavrikakis, S. Scott, T. Kuech, J. Dumesic, Angew. Chem. Int. Ed. Engl. 52 (2013) 13808–13812.
[8] J. Lu, B. Liu, J. Greeley, Z. Feng, J. Libera, Y. Lei, M. Bedzyk, P. Stair, J. Elam, Chem. Mater. 24 (2012) 2047–2055.
[9] (a) X. Liang, J. Li, M. Yu, C. McMurray, J. Falconer, A. Weimer, ACS Catal. 1 (2011) 1162–1165;
(b) J. Lu, B. Fu, M.C. Kung, G. Xiao, J. Elam, H. Kung, P.C. Stair, Science 335 (2012) 1205–1208.
[10] S. George, Chem. Rev. 110 (2010) 111–131.
[11] R. Johnson, A. Hultqvist, S. Bent, Mater. Today 17 (2014) 236–246.
[12] C. Travis, R. Adomaitis, Theor. Chem. Acc. 133 (2013) 1–11.
[13] (a) H. Feng, J. Libera, P. Stair, J. Miller, J. Elam, ACS Catal. 1 (2011) 665–673;
(b) V. Anderson, N. Leick, J. Clancey, K. Hurst, K. Jones, A. Dillon, S. George, J. Phys. Chem. C 118 (2014) 8960–8970;
(c) A. Goulas, J.J. van Ommen, Mater. Chem. A 1 (2013) 4647–4650 (and references therein).
[14] (a) T. Aaltonen, M. Ritala, T. Sajavaara, J. Keinonen, M. Leskelä, Chem. Mater. 15 (2003) 1924–1928;
(b) H. Feng, J. Elam, J. Libera, W. Setthapun, P. Stair, Chem. Mater. 22 (2010) 3133–3142.

[15] S. Christensen, J. Elam, Chem. Mater. 22 (2010) 2517–2525.
[16] (a) K. Cao, Q. Zhu, B. Shan, R. Chen, Nature 5 (2015) 1–7;
(b) M. Weber, A. Mackus, M. Verheijen, C. van der Marel, W. Kessels, Chem. Mater. 24 (2012) 2973–2977.
[17] S. Sun, G. Zhang, N. Gauquelin, N. Chen, J. Zhou, S. Yang, W. Chen, X. Meng, D. Geng, M.N. Banis, R. Li, S. Ye, S. Knights, G. Botton, T.-K. Sham, X. Sun, Nature 3 (2013) 1–9.
[18] J. Camacho-Bunquin, H. Shou, P. Aich, D. Beaulieu, H. Klotzsch, H. Bachman, C. Marshall, A. Hock, P. Stair, Rev. Sci. Inst. 86 (2015) 084103.
[19] L. Zhuravlev, Langmuir 3 (1987) 316–318.
[20] L. Zhuravlev, Colloids Surf. A 173 (2000) 1–38.
[21] V. Potapov, L. Zhuravlev, Glass Phys. Chem. 31 (2005) 661–670.
[22] (a) T. Tynell, M. Karppinen, Semicond. Sci. Technol. 29 (2014) 043001, 1–15;
(b) D. Lee, S. Kim, S. Noh, J. Nanosci. Nanotechnol. 11 (2011) 4312–4316;
(c) E. Guziewicz, M. Godlewski, T. Krajewski, Ł. Wachnicki, A. Szczepanik, K. Kopalko, A. Wójcik-Głodowska, E. Przeździecka, W. Paszkowicz, E. Łusakowska, P. Kruszewski, N. Huby, G. Tallarida, S. Ferrari, J. Appl. Phys. 105 (2009) 122413, 1–5;
(d) C.-H. Ku, J.-M. Huang, C.-M. Lin, H.-Y. Lee, Thin Solid Films 518 (2009) 1373–1376.
[23] A. Becke, J. Chem. Phys. 98 (1993) 5648–5652.
[24] M. Frisch, G. Trucks, H. Schlegel, G. Scuseria, M. Robb, J. Cheeseman, G. Scalmani, V. Barone, B. Mennucci, G. Petersson, H. Nakatsuji, M. Caricato, X. Li, H. Hratchian, A. Izmaylov, J. Bloino, G. Zheng, J. Sonnenberg, M. Hada, M. Ehara, K. Toyota, R. Fukuda, J. Hasegawa, M. Ishida, T. Nakajima, Y. Honda, O. Kitao, H. Nakai, T. Vreven, J. Montgomery Jr., J. Peralta, F. Ogliaro, M. Bearpark, J. Heyd, E. Brothers, K. Kudin, V. Staroverov, R. Kobayashi, J. Normand, K. Raghavachari, A. Rendell, J. Burant, S. Iyengar, J. Tomasi, M. Cossi, N. Rega, N. Millam, M. Klene, J. Knox, J. Cross, V. Bakken, C. Adamo, J. Jaramillo, R. Gomperts, R. Stratmann, O. Yazyev, A. Austin, R. Cammi, C. Pomelli, J. Ochterski, R. Martin, K. Morokuma, V. Zakrzewski, G. Voth, P. Salvador, J. Dannenberg, S. Dapprich, A. Daniels, Ö. Farkas, J. Foresman, J. Ortiz, J. Cioslowski, D. Fox, Gaussian 09, Revision D.01, Gaussian Inc., Wallingford, CT, 2009.
[25] H. Hratchian, H. Schlegel, J. Chem. Theory Comput. 1 (2005) 61–69.
[26] A. Schafer, C. Huber, R. Ahlrichs, J. Chem. Phys. 100 (1994) 5829–5835.
[27] F. Jiang, J. Huang, L. Niu, G. Xiao, Catal. Lett. 145 (2015) 947–954.
[28] S. Kucheyev, J. Biener, Y. Wang, T. Baumann, K. Wu, T. van Buuren, A. Hamza, J. Satcher, J. Elam, M. Pellin, J. Appl. Phys. Lett. 86 (2005) 083108-1–083108-3.
[29] F. Wang, W. Xiao, G. Xiao, Catal. Lett. 145 (2015) 860–867.
[30] Z. Baji, Z. Lábadi, Z.E. Horváth, G. Molnár, J. Volk, I. Bársony, P. Bársony, *Cryst. Growth Des.* 12 (2012) 5615–5620.
[31] A. Dent, R. Kokes, J. Phys. Chem. 73 (1969) 3772–3780.
[32] A. Dent, R. Kokes, J. Phys. Chem. 73 (1969) 3781–3790.
[33] A. Dent, R. Kokes, J. Phys. Chem. 74 (1970) 3653–3662.
[34] W. Conner, R. Innes, R.J. Kokes, J. Am. Chem. Soc. 90 (1968), 6858–6858.
[35] A. Dent, R. Kokes, J. Am. Chem. Soc. 91 (1969) 7207–7208.
[36] S. Vettel, A. Vaupel, P. Knochel, Tet. Lett. 36 (1995) 1023–1026.
[37] Y. Gao, H. Urabe, F. Sato, J. Org. Chem. 59 (1994) 5521–5523.
[38] D. King, X. Liang, P. Li, A. Weimer, Thin Solid Films 516 (2008) 8517–8523.
[39] H. Berndt, G. Lietz, B. Lücke, J. Völter, Appl. Catal. A 146 (1996) 351–363.
[40] (a) Z. Zhao, C. Chiub, J. Gong, Chem. Sci. 6 (2015) 4403–4425;
(b) F. Li, H. Yang, T. Ju, X. Li, C. Hu, Int. J. Mol. Sci. 13 (2012) 9278–9297;
(c) R. Perutz, S. Sabo-Etienne, Angew. Chem. Int. Ed. Engl. 46 (2007) 2578–2592;
(d) E. Heracleous, M. Machli, A. Lemonidou, I. Vasalos, J. Mol. Catal. A: Chem. 232 (2005) 29–39.
[41] E. Rassy, A. Pierre, J. Non-Cryst. Solids 351 (2005) 1603–1610.
[42] B. Keyes, L. Gedvilas, X. Li, T. Coutts, J. Cryst. Growth 281 (2005) 297–302.
[43] M. Westerhausen, A. Kneifel, A. Kalisch, Angew. Chem. Int. Ed. 44 (2005) 96–98.
[44] (a) A. Lesage, Phys. Chem. Chem. Phys. 11 (2009) 6876–6891;
(b) R. Faulkner, J. DiVerdi, Y. Yang, T. Kobayashi, G. Maciel, Materials 6 (2013) 18–46;
(c) J. Trébosc, J. Wiench, S. Huh, V. Lin, M. Pruski, J. Am. Chem. Soc. 127 (2005) 3057–3068;
(d) W. Einholz, W. Gollinger, W.Z. Haubold, Naturforsch. B Chem. Sci. 45 (1990) 25–30.
[45] J. Eriksson, P.I. Arvidsson, Ö. Davidsson, Chem. Eur. J. 5 (1999) 2356–2361.
[46] J. Bacsa, F. Hanke, S. Hindley, R. Odedra, G.R. Darling, A.C. Jones, A. Steiner, Angew. Chem. Int. Ed. Engl. 50 (2011) 11685–11687.
[47] K. Tohji, Y. Udagawa, T. Mizushima, A. Ueno, J. Phys. Chem. 89 (1985) 5671–5676.
[48] L.M. Lamberti, J. Phys. D Appl. Phys. 46 (2013) 423001.
[49] A.B. Getsoian, U. Das, J. Camacho-Bunquin, G. Zhang, J.R. Gallagher, B. Hu, S. Cheah, J.A. Schaidle, D.A. Ruddy, J.E. Hensley, T.R. Krause, L.A. Curtiss, J.T. Miller, A.S. Hock, Organometallic model complexes elucidate the active gallium species in alkane dehydrogenation catalysts based on ligand effects in Ga K-edge XANES, Catal. Sci. Technol. (2016), http://dx.doi.org/10.1039/C6CY00698A.